

Temperature-sensing array using the metal-to-insulator transition of $\text{Nd}_x\text{Sm}_{1-x}\text{NiO}_3$

Fengbo Yan, Ziang Li, Hao Zhang, Yuchen Cui, Kaiqi Nie, Nuofu Chen, and Jikun Chen

Cite this article as:

Fengbo Yan, Ziang Li, Hao Zhang, Yuchen Cui, Kaiqi Nie, Nuofu Chen, and Jikun Chen, Temperature-sensing array using the metal-to-insulator transition of $\text{Nd}_x\text{Sm}_{1-x}\text{NiO}_3$, *Int. J. Miner. Metall. Mater.*, 31(2024), No. 7, pp. 1694-1700. <https://doi.org/10.1007/s12613-023-2816-1>

View the article online at [SpringerLink](#) or [IJMMM Webpage](#).

Articles you may be interested in

Ying-zhi Chen, Dong-jian Jiang, Zheng-qi Gong, Jing-yuan Li, and Lu-ning Wang, [Anodized metal oxide nanostructures for photoelectrochemical water splitting](#), *Int. J. Miner. Metall. Mater.*, 27(2020), No. 5, pp. 584-601. <https://doi.org/10.1007/s12613-020-1983-6>

Shuang Huang, Hua-lan Xu, Sheng-liang Zhong, and Lei Wang, [Microwave hydrothermal synthesis and characterization of rare-earth stannate nanoparticles](#), *Int. J. Miner. Metall. Mater.*, 24(2017), No. 7, pp. 794-803. <https://doi.org/10.1007/s12613-017-1463-9>

Jing-qun Yin, Zhi-qiang Zou, and Jun Tian, [Preparation of crystalline rare earth carbonates with large particle size from the lixivium of weathered crust elution-deposited rare earth ores](#), *Int. J. Miner. Metall. Mater.*, 27(2020), No. 11, pp. 1482-1488. <https://doi.org/10.1007/s12613-020-2066-4>

Sushma Miryala and Masato Murakami, [Special variation of infiltration-growth processed bulk YBCO fabricated using new liquid source: \$\text{Ba}_3\text{Cu}_5\text{O}_8\$ \(1:1.3\) and \$\text{YbBa}_2\text{Cu}_3\text{O}_y\$](#) , *Int. J. Miner. Metall. Mater.*, 28(2021), No. 6, pp. 1048-1056. <https://doi.org/10.1007/s12613-020-2213-y>

Jing Zhou, Dan-dan Nie, Xian-bo Jin, and Wei Xiao, [Controllable nitridation of \$\text{Ta}_2\text{O}_5\$ in molten salts for enhanced photocatalysis](#), *Int. J. Miner. Metall. Mater.*, 27(2020), No. 12, pp. 1703-1710. <https://doi.org/10.1007/s12613-020-2050-z>

Sheng-hua Yin, Lei-ming Wang, Xun Chen, and Ai-xiang Wu, [Agglomeration and leaching behaviors of copper oxides with different chemical binders](#), *Int. J. Miner. Metall. Mater.*, 28(2021), No. 7, pp. 1127-1134. <https://doi.org/10.1007/s12613-020-2081-5>



IJMMM WeChat



QQ author group

Temperature-sensing array using the metal-to-insulator transition of $\text{Nd}_x\text{Sm}_{1-x}\text{NiO}_3$

Fengbo Yan¹, Ziang Li¹, Hao Zhang², Yuchen Cui¹, Kaiqi Nie³, Nuofu Chen², and Jikun Chen¹✉

1) School of Materials Science and Engineering, University of Science and Technology Beijing, Beijing 100083, China

2) School of Renewable Energy, North China Electric Power University, Beijing 102206, China

3) Beijing Synchrotron Radiation Facility, Institute of High Energy Physics, Chinese Academy of Sciences, Beijing 100049, China

(Received: 18 August 2023; revised: 21 December 2023; accepted: 22 December 2023)

Abstract: Rare-earth nickelates (RENiO_3) show widely tunable metal-to-insulator transition (MIT) properties with ignorable variations in lattice constants and small latent heat across the critical temperature (T_{MIT}). Particularly, it is worth noting that compared with the more commonly investigated vanadium oxides, the MIT of RENiO_3 is less abrupt but usually across a wider range of temperatures. This sheds light on their alternative applications as negative temperature coefficient resistance (NTCR) thermistors with high sensitivity compared with the current NTCR thermistors, other than their expected use as critical temperature resistance thermistors. In this work, we demonstrate the NTCR thermistor functionality for using the adjustable MIT of $\text{Nd}_x\text{Sm}_{1-x}\text{NiO}_3$ within 200–400 K, which displays larger magnitudes of NTCR (e.g., more than 7%/K) that is unattainable in traditional NTCR thermistor materials. The temperature dependence of resistance ($R-T$) shows sharp variation during the MIT of $\text{Nd}_x\text{Sm}_{1-x}\text{NiO}_3$ with no hysteresis via decreasing the Nd content (e.g., $x \leq 0.8$), and such a $R-T$ tendency can be linearized by introducing an optimum parallel resistor. The sensitive range of temperature can be further extended to 210–360 K by combining a series of $\text{Nd}_x\text{Sm}_{1-x}\text{NiO}_3$ with eight rare-earth co-occupation ratios as an array, with a high magnitude of NTCR (e.g., 7%–14%/K) covering the entire range of temperatures.

Keywords: rare-earth nickelates; metal-to-insulator transition; correlated oxides; perovskites

1. Introduction

The metal-to-insulator transition (MIT) achieved in 3d-correlated transitional metal oxides prompts abrupt variations in the electronic and/or optical properties beyond conventional semiconductors, enabling applications such as critical temperature resistance thermistors, correlated logical devices, and thermochromism [1–6]. Among the MIT material family, rare-earth nickelates (RENiO_3) exhibit an exceptionally complex electronic phase diagram and multiple electronic phase transitions. For instance, a reversible charge disproportionation (or antidisproportionation) related to the $\text{Ni}^{3+} \leftrightarrow \text{Ni}^{(3\pm 0)+}$ occurs across a critical temperature (T_{MIT}) that prompts the conventional MIT properties of RENiO_3 . An overwhelming advantage in the MIT of RENiO_3 is the wide and continuous tunability in T_{MIT} (e.g., within 100–600 K) by simply adjusting its rare-earth composition. For example, reducing the rare-earth ionic radius (r_{RE}) within RENiO_3 weakens the orbital overlapping between Ni 3d and O 2p, which increases the relative stability of the insulating phase compared with the metallic phase and thus increases T_{MIT} [7]. Aside from the conventional MIT, the 3d orbital configuration of Ni can be further switched among Ni^{3+} ($t_{2g}^6 e_g^1$), Ni^{2+} ($t_{2g}^6 e_g^2$) and Ni^{1+} ($t_{2g}^6 e_g^3$) via a hydrogen (or lithium)-related

Motronic process. Direct manipulation of the orbital occupancy leads to the further discovery of novel electronic phases within RENiO_3 , such as the electronically highly correlated phase associated with Ni^{2+} and the nickelate superconductor corresponding to Ni^+ [8]. The abundant electronic states of RENiO_3 provide a new paradigm for further exploring emerging electronic applications such as proton-doped memory devices [9–11], synaptic devices [12–14], and reconfigurable perovskite devices [15].

Nevertheless, the present application of RENiO_3 merely focuses on a single device pixel at a destined rare-earth composition, while their further array application via integrating RENiO_3 with different rare-earth compositions has not yet been fully explored. It is worth noting that precise control in the ground electronic phase of RENiO_3 can be realized by adjusting the co-occupation ratio of two rare-earth elements, which determines the average magnitude of r_{RE} . This was previously shown by the linear variation in the T_{MIT} of $\text{Nd}_x\text{Sm}_{1-x}\text{NiO}_3$ with the rare-earth co-occupation atomic ratio x . Thus, establishing arrays of multiple RENiO_3 pixels offers new freedom from the perspective of their electronic permutation and combination in further extending their correlated electronic applications.

In this work, a method was proposed to achieve precise

✉ Corresponding author: Jikun Chen E-mail: jikunchen@ustb.edu.cn

© University of Science and Technology Beijing 2024

temperature measurement using the negative temperature coefficient resistance (NTCR) of RENiO_3 within the MIT region. Compared with a conventional NTCR thermistor, RENiO_3 displays a larger temperature coefficient resistance (TCR) due to the abrupt transition from an insulator to a metal when reaching a critical temperature. Thus, it is anticipated that the use of RENiO_3 for temperature measurement would give a higher accuracy and sensitivity. However, hysteresis exists in the resistance curves as a function of temperature for some RENiO_3 with a single rare-earth composition (e.g., NdNiO_3). As a consequence, we selected and prepared $\text{Nd}_x\text{Sm}_{1-x}\text{NiO}_3$ with different Nd/Sm atomic ratios ($x = 0.2, 0.33, 0.4, 0.5, 0.6, 0.67, 0.75, 0.8, \text{ and } 1$). Their temperature dependence on resistance (R - T) exhibits sharp MIT variation across a temperature range of 200–400 K with no hysteresis except for $x = 1$. In addition, for $\text{Nd}_x\text{Sm}_{1-x}\text{NiO}_3$ with various x , their total resistance after paralleling an optimum constant resistor indeed varied linearly with temperature within a specific temperature range. In addition, the linear coefficient of total resistance with temperature was much larger in $\text{Nd}_x\text{Sm}_{1-x}\text{NiO}_3$ than that in conventional NTCR thermistors because of larger magnitudes of NTCR that originate from their sharp MIT and is unachievable in conventional NTCR thermistor materials. Thus, it can be expected that integrating an array of $\text{Nd}_x\text{Sm}_{1-x}\text{NiO}_3$ with different x values can be applied to measure the temperature with high sensitivity and precision in the future.

2. Experimental

2.1. Sample preparation

$\text{Nd}_x\text{Sm}_{1-x}\text{NiO}_3$ powders with $x = 0, 0.2, 0.33, 0.4, 0.5, 0.6, 0.67, 0.75, 0.8, \text{ and } 1$ were prepared using the KCl molten salt-assisted high oxygen pressure reaction approach reported in our previous work [16]. Typically, rare-earth oxides ($\text{Nd}_2\text{O}_3, \text{Sm}_2\text{O}_3$), NiO, and KCl were mixed and ground at a molar ratio of 1:2:2 in an agate mortar. The obtained mixture was transferred into a quartz tube and then calcined at 800°C and 10 MPa oxygen pressure for 24 h. Next, the obtained powder was rinsed with deionized water and ethanol to remove KCl and residual water. Finally, the powder was pressed into pellets and further sintered at 800°C and 10 MPa oxygen pressure for 24 h.

2.2. Characterization

The crystal structures of the as-prepared $\text{Nd}_x\text{Sm}_{1-x}\text{NiO}_3$ powders were verified by X-ray diffraction (XRD, Rigaku SmartLab). The lattice constants of $\text{Nd}_x\text{Sm}_{1-x}\text{NiO}_3$ were measured by Rietveld refinement using FullProf software. The morphologies of the samples were characterized by scanning electron microscopy (SEM) with a JEOL JSM 6510A electron microscope. Near-edge X-ray absorption fine structure (NEXAFS) was conducted at the BSRF-4b9b beamline of the Beijing Synchrotron Radiation Facility, Institute of High Energy Physics, Chinese Academy of Sciences to reflect the electronic structures of $\text{Nd}_x\text{Sm}_{1-x}\text{NiO}_3$.

The resistance as a function of temperature for $\text{Nd}_x\text{Sm}_{1-x}\text{NiO}_3$ was determined from 5 to 300 K using a physical property measurement system (Quantum Design Inc., China) and above 300 K using a commercialized CTA system.

3. Results and discussion

3.1. Initial concepts

As illustrated in Fig. 1(a), $\text{Nd}_x\text{Sm}_{1-x}\text{NiO}_3$ shows a distorted perovskite and continuously tunable T_{MIT} by simply adjusting the Nd/Sm ratios (x from 1 to 0) within 200–400 K. It is worth noting that the resistivity of RENiO_3 exhibits an abrupt drop across the transition temperature T_{MIT} by 1–3 order within a wide temperature range compared with the conventional NTCR thermistor [17–19], as shown in Fig. 1(b). Moreover, another characteristic of RENiO_3 with middle and heavy rare-earth composition is that there is nearly no thermally induced hysteresis in their MIT when measuring the temperature dependence of resistivity by heating up and cooling down. Thus, compared with the conventional NTCR thermistor, the larger decrease of resistance in the MIT region from Fig. 1(b) would result in higher TCR, where the resistance of RENiO_3 is more sensitive to temperature changes. Hence, it is expected that using RENiO_3 for temperature measurements will lead to higher accuracy and sensitivity. However, it is worth mentioning that the nonlinear variation of resistance with the temperature of RENiO_3 in the MIT region would be unfavorable for actual temperature measurements. To solve this problem, an optimum constant resistor was paralleled to RENiO_3 , which causes the total resistance to show a linear change within a certain temperature range. Then, it can be utilized to determine the temperature using the typical electric circuit diagram shown in Fig. 1(c). The circuit (red box in Fig. 1(c)) is a constant voltage source that gives a stable voltage for the bridge voltage sampling part (blue box). The bridge voltage sampling part is employed to obtain the total resistance of rare-earth nickelates and R_p in parallel. Once the total resistance is probed, the temperature can be determined on the basis of the assumption that the total resistance varies linearly with temperature. Afterward, the voltage amplification part (purple box) magnifies the weak voltage signals between V_1 and V_2 . Also, it would be better to integrate an array containing a series of RENiO_3 with different rare-earth compositions to realize precise temperature measurements over a wide temperature range.

3.2. Material structure, morphology, and electronic structure

To achieve the above concept, a series of $\text{Nd}_x\text{Sm}_{1-x}\text{NiO}_3$ powders with different rare-earth compositions ($x = 0, 0.2, 0.33, 0.4, 0.5, 0.6, 0.67, 0.75, 0.8, \text{ and } 1$) were synthesized and then pressed into pellets (more details in the Section 2). Fig. 2(a) displays the XRD patterns of the as-synthesized $\text{Nd}_x\text{Sm}_{1-x}\text{NiO}_3$ samples. Almost all peaks for each $\text{Nd}_x\text{Sm}_{1-x}\text{NiO}_3$ sample are in accordance with the standard

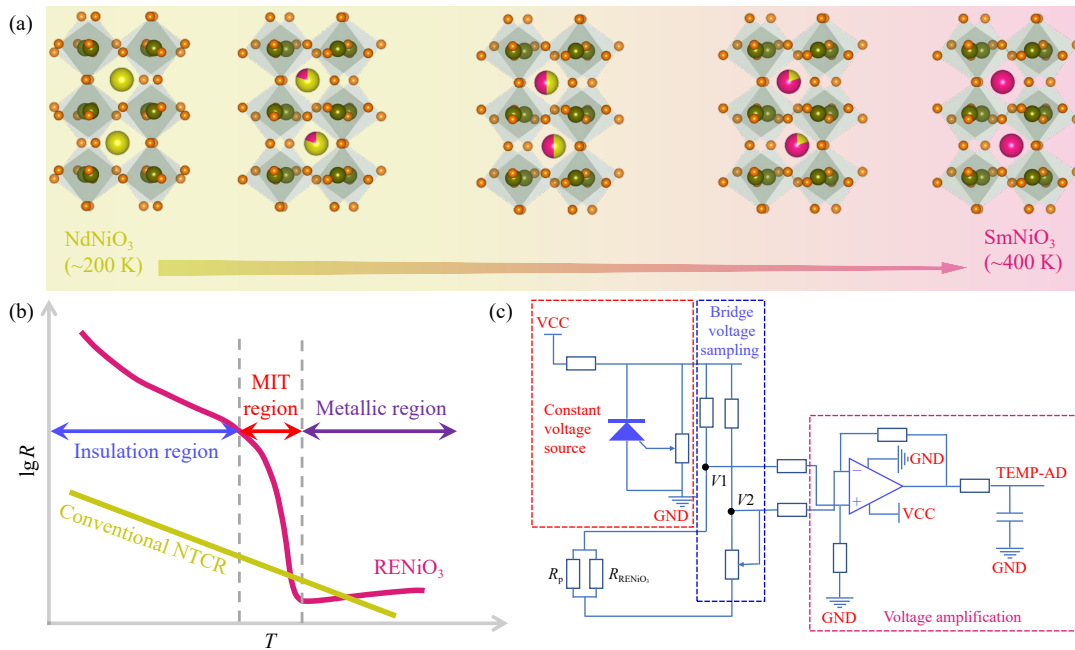


Fig. 1. (a) Schematic of the crystal structures of $RENiO_3$ with different Nd/Sm ratios. (b) Comparison of resistance versus temperature for $RENiO_3$ and conventional NTCR. (c) Possible electric circuit for temperature measurement using linearized $RENiO_3$ (VCC—Volt current condenser; GND—ground; TEMP-AD—temperature analog-to-digital converter; $V1$ and $V2$ —voltage 1 and voltage 2; R_p and R_{RENiO_3} —parallel resistance and resistance of $RENiO_3$).

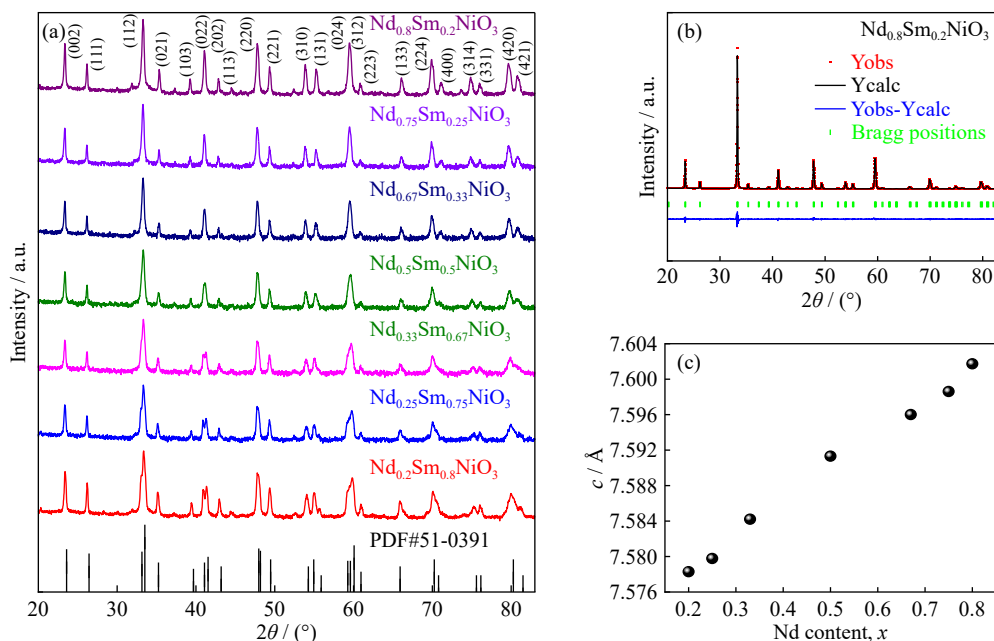


Fig. 2. (a) XRD patterns of the as-prepared $Nd_xSm_{1-x}NiO_3$ powders (PDF#51-0391) covered with different rare-earth compositions ($x = 0.2, 0.25, 0.33, 0.5, 0.67, 0.75, \text{ and } 0.8$). (b) Rietveld refinement patterns obtained from the measured XRD spectra for $Nd_{0.8}Sm_{0.2}NiO_3$ (Yobs and Ycalc are measured XRD pattern and rietveld refinement pattern, respectively). The red lines indicate the obtained XRD data, the black lines indicate the calculated pattern, the blue lines refer to the observed calculated pattern, and the green vertical ticks indicate the positions of the Bragg reflections. (c) Variation of the c -axis lattice parameters of the as-prepared $Nd_xSm_{1-x}NiO_3$ powder with increasing Nd content, which was obtained from the Rietveld refinement of the X-ray diffraction spectra.

PDF card (PDF#51-0391), demonstrating a typical distorted perovskite structure. As a typical example, the XRD spectrum of $Nd_{0.8}Sm_{0.2}NiO_3$ was refined using the Rietveld method, as shown in Fig. 2(b) (see more Rietveld refinements for other $Nd_xSm_{1-x}NiO_3$ in Fig. S1). Some parameters taken from the Rietveld refinements are summarized in Table S1. R_p and

χ^2 factors are less than 5.6% and 3.5%, respectively, for $Nd_xSm_{1-x}NiO_3$, which shows the effectiveness of the Rietveld refinements. In addition, the lattice constants of the c -axis (c) obtained from the Rietveld refinements of the as-made $Nd_xSm_{1-x}NiO_3$ samples increase with the improvement of the Nd content, as shown in Fig. 2(c). These results align

with the fact that SmNiO_3 has a smaller lattice parameter than NdNiO_3 [20].

The morphologies of the $\text{Nd}_x\text{Sm}_{1-x}\text{NiO}_3$ samples were further observed by using SEM. As a representative example, Fig. 3(a) and (b) shows the morphologies of the as-synthesized $\text{Nd}_{0.67}\text{Sm}_{0.33}\text{NiO}_3$ powder and the corresponding cross-section, respectively. The morphology of the $\text{Nd}_{0.67}\text{Sm}_{0.33}\text{NiO}_3$ powder in Fig. 3(a) shows a typical cubic shape. The size is about several micrometers, which is close to our previous results [7]. Also, based on the energy dispersive spectroscopy results, the practical composition of the as-synthesized powders agrees with their respective nominal compositions, as shown in Fig. S2 for $\text{Nd}_{0.67}\text{Sm}_{0.33}\text{NiO}_3$ powder. In addition, a compact cross-section was observed for the sintered pellets, as shown in Fig. 3(b). It is worth noting that although grains of different sizes are observed in the cross-section of the pellet, their composition is the same, as shown in Fig. S3. The dense pellet also gives convenience for measuring electrical transportation.

Next, the electronic structures of $\text{Nd}_x\text{Sm}_{1-x}\text{NiO}_3$ with different rare-earth compositions were analyzed by NEXAFS, and the O-K edge and Ni-L₃ edge spectra are presented in Fig. 3(c) and (d), respectively. Comparing the O-K edge of NdNiO_3 and $\text{Nd}_{0.8}\text{Sm}_{0.2}\text{NiO}_3$ with that of $\text{Nd}_{0.2}\text{Sm}_{0.8}\text{NiO}_3$, an improvement of the prepeak (marked as A) can be observed

in Fig. 3(c) when increasing the Nd content. It has been reported in previous literature [21] that the intensity of prepeak A in their O-K edge spectra reflects the overlapping between Ni 3d and O 2p orbitals. Thus, a higher intensity of prepeak A is associated with a larger overlap between Ni 3d and O 2p and Ni–O–Ni bond angle, which stabilizes the metallic phase of RENiO_3 and results in a lower T_{MIT} . Further consistency can be verified from the variations in their Ni-L₃ spectra (Fig. 3(d)). The relative intensity of peak A compared with that of peak B shows the proportion of the Ni^{3+} orbital configurations [22]. In Fig. 3(d), an increasing intensity of peak A is observed with increasing Nd content. In general, the Ni^{3+} orbital configuration is associated with metallic states, causing a decrease in T_{MIT} when Nd content is increased [19].

3.3. MIT properties and potential applications for temperature sensing

In addition, the resistance (R) as a function of temperature (T) (R - T) curves for the as-synthesized $\text{Nd}_x\text{Sm}_{1-x}\text{NiO}_3$ during both heating and cooling processes are presented in Fig. 4(a). All samples show significant MIT behaviors, and the decrease in resistance in the MIT region reaches approximately two orders of magnitude. Furthermore, it can be noted that their electrical transport curves measured by heating and cooling procedures overlap well, except for NdNiO_3 ,

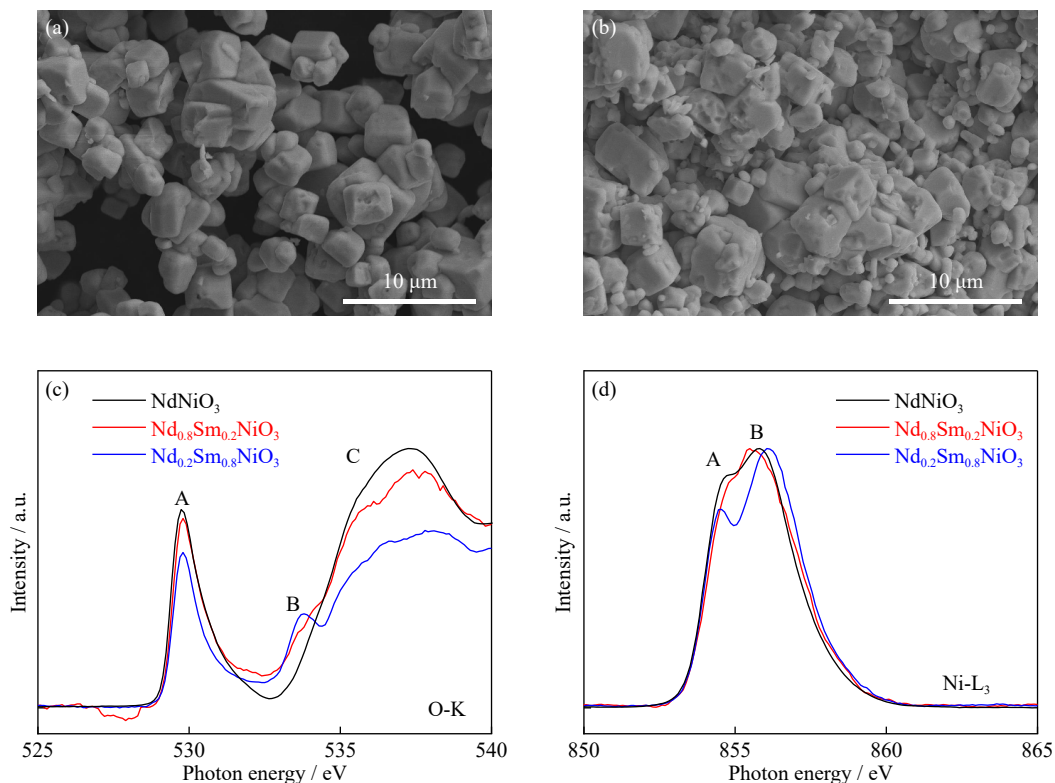


Fig. 3. Scanning electron microscope images of (a) the $\text{Nd}_{0.67}\text{Sm}_{0.33}\text{NiO}_3$ powder and (b) the cross-section of the $\text{Nd}_{0.67}\text{Sm}_{0.33}\text{NiO}_3$ pellet. NEXAFS analysis of the (c) O-K edge and (d) Ni-L₃ edge of $\text{Nd}_x\text{Sm}_{1-x}\text{NiO}_3$ with $x = 1, 0.8, \text{ and } 0.2$. In (c), peak A, also called the prepeak, is associated with the transition from O 1s to the Ni 3d-O 2p hybridized states. Peak B results from the 4f and 5d hybridized states of rare-earth ions with O 2p. Peak C corresponds to the Ni 4s and 4p hybridized with O 2p. In (d), the Ni-L₃ spectrum originates from the Ni 2p to Ni 3d transition and splits into peaks A and B. The proportion of the $t_{2g}^6 e_g^1$ (Ni^{3+}) orbital configurations compared with the $t_{2g}^6 e_g^2$ (Ni^{2+}) configuration is indicated by the relative height of peak B split from peak A in the Ni-L₃ NEXAFS spectrum.

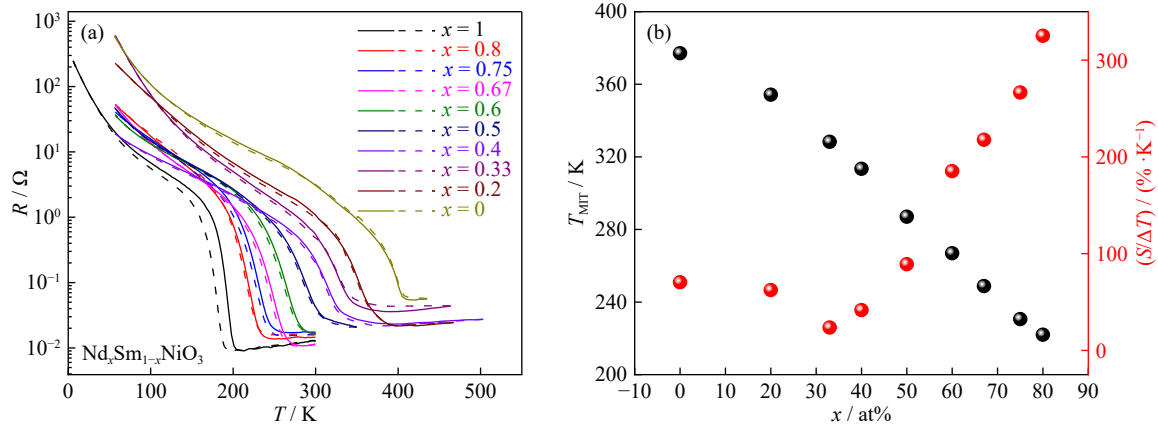


Fig. 4. (a) R - T curves of rare-earth nickelates $\text{Nd}_x\text{Sm}_{1-x}\text{NiO}_3$ pellets with different rare-earth compositions ($x = 1, 0.8, 0.75, 0.67, 0.6, 0.5, 0.4, 0.33, 0.2,$ and 0). The data source of $x = 1$ is taken elsewhere [23]. Solid lines refer to the heating process, while the dashed lines refer to the cooling process. (b) Variation of T_{MIT} and $S/\Delta T$ with the Nd content. Fig. S4 shows the detailed process of calculating using $S/\Delta T$, and $S = R_I/R_M$, where R_I and R_M stand the resistances of the insulating phase I and the metallic phase M , respectively.

which offers the prerequisite for temperature measurement because the presence of a gap between the heating and cooling curves makes the measurement of temperature inaccurate. Thus, the subsequent discussion will not include NdNiO_3 . The decreasing tendency of T_{MIT} with increasing Nd in Fig. 4(b) proves the correct analysis of the electronic structure of the as-synthesized $\text{Nd}_x\text{Sm}_{1-x}\text{NiO}_3$. In addition, Fig. 4(b) displays the variations (R_I/R_M)/ ΔT (i.e., $S/\Delta T$) with the improvement of Nd percentage, to some degree, indicating the sharpness of MIT. Note that a more abrupt MIT tendency can be found when increasing the Nd proportion, but interestingly, the sharpness of the MIT behavior increases slightly when the portion of Nd continues to decrease to below 30at%.

Nevertheless, the nonlinear resistance variation with temperature for $\text{Nd}_x\text{Sm}_{1-x}\text{NiO}_3$ within the MIT region is not beneficial for measuring the temperature directly and accurately. Thus, a suitable constant resistor is needed in parallel with $\text{Nd}_x\text{Sm}_{1-x}\text{NiO}_3$ to linearize their R - T curves within a specific temperature range of MIT. Concrete linearization details can be found in Section 3 of the supporting information. To demonstrate the possibility of the linearization method, we selected $\text{Nd}_{0.8}\text{Sm}_{0.2}\text{NiO}_3$ as a representative example to show the linearization process within the MIT region. Fig. 5(a) illustrates the resistance of $\text{Nd}_{0.8}\text{Sm}_{0.2}\text{NiO}_3$ as a function of temperature, displaying significant MIT behavior, as shown in the red box. Combined with the linearization method in the supplementary material, we chose this R - T curve included in the red box to be linearized, and the obtained results are shown in Fig. 5(b). It can be clearly observed that the R - T curve of $\text{Nd}_{0.8}\text{Sm}_{0.2}\text{NiO}_3$ deviates from the linear relationship without paralleling a constant resistor, whereas a linear tendency of resistance with temperature appears with the addition of an optimum constant resistor. This linear tendency proves the validity of the linearization method. However, it is also worth mentioning that the linear variation in the temperature dependence of resistance across the MIT of a single $\text{Nd}_{1-x}\text{Sm}_x\text{NiO}_3$ composition usually covers an

effective temperature range of several tens of Kelvin. Thus, a series of $\text{Nd}_{1-x}\text{Sm}_x\text{NiO}_3$ ($x = 0.2, 0.33, 0.4, 0.5, 0.6, 0.67, 0.75, 0.8$) can be connected in parallel as an array to cover the entire temperature range of 210–360 K. By further applying this linear method to $\text{Nd}_x\text{Sm}_{1-x}\text{NiO}_3$ with other rare-earth compositions, some sensing temperature parameters such as linear slopes, magnitude of the parallel resistor, and linear temperature ranges can be determined [24]. The relationships among these parameters are summarized in Fig. 5(c). Since the magnitudes of slope k are associated with the resistance of $\text{Nd}_x\text{Sm}_{1-x}\text{NiO}_3$ at the linearization temperature, as elucidated in Section 3 of the supplementary material, we introduced the ratio k/R_T as a novel and scientifically derived parameter to reflect the sensitivity of the total resistance to temperature variation, where R_T is the resistance of $\text{Nd}_x\text{Sm}_{1-x}\text{NiO}_3$ at the linearization temperature, which is different for each x value. Nevertheless, if the linearization temperature is determined for a certain x value, R_T is a constant. The variation tendency of k/R_T with Nd content is consistent with the evolution of $S/\Delta T$ as a function of temperature, as shown in Fig. 4(c). Meanwhile, we also calculated the TCR for the as-synthesized $\text{Nd}_{1-x}\text{Sm}_x\text{NiO}_3$ shown in Fig. S6. The maximum TCRs of every sample are shown in Fig. 5(d). It can be observed that the variations of TCR and k/R_T as a function of Nd are consistent, which agrees well with our expectation that a larger TCR means a higher temperature sensitivity. Furthermore, the same TCR values are difficult to achieve in a conventional NTCR thermistor. In other words, integrating an array of $\text{Nd}_x\text{Sm}_{1-x}\text{NiO}_3$ with various x values allows for precise and highly sensitive temperature measurements in the future. The process of temperature measurement can be explained more specifically as follows: the target temperature range can be first detected by the temperature dependence of RENiO_3 with a heavier rare-earth composition (e.g., GdNiO_3) that shows insulator transportation. Subsequently, the system is switched to the specific composition of $\text{Nd}_x\text{Sm}_{1-x}\text{NiO}_3$ to realize accurate temperature sensing within the low-temperature range.

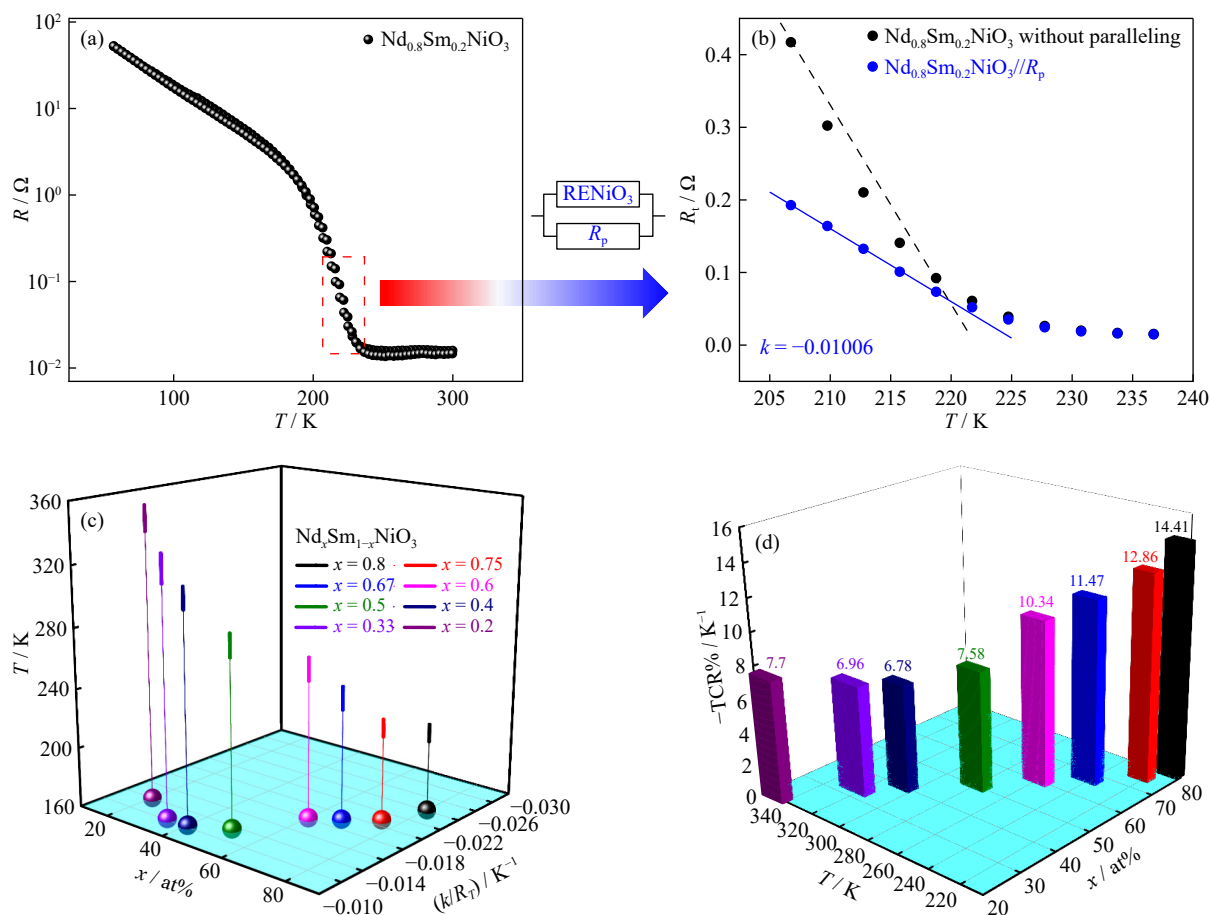


Fig. 5. (a) Representative temperature dependence of the resistance of $\text{Nd}_{0.8}\text{Sm}_{0.2}\text{NiO}_3$ for linearity in temperature sensing. The red dashed box means that this part of the R – T curve is selected to achieve linearization by paralleling the constant resistor. (b) Before and after paralleling a specific constant resistor, the variations of the total resistance R_t with temperature. The black dashed line indicates that the curve will deviate from the linear relationship without paralleling a constant resistance in the same temperature range. The blue solid line is the linear fitting curve, and k is its slope. R_t is the total resistance of $\text{Nd}_{0.8}\text{Sm}_{0.2}\text{NiO}_3$ or $\text{Nd}_{0.8}\text{Sm}_{0.2}\text{NiO}_3$ parallel to R_p . (c) Linear temperature ranges and k/R_t for various rare-earth nickelates. (d) Temperature coefficient resistance (TCR) maxima and linear temperature range for different rare-earth nickelates.

4. Conclusion

In conclusion, we propose a strategy to sense low-range temperatures using the MIT properties of array-like RENiO_3 , where high magnitudes of TCR can be realized beyond conventional NTCR materials. A series of $\text{Nd}_x\text{Sm}_{1-x}\text{NiO}_3$ samples with different rare-earth compositions of $x = 0$ – 1 were synthesized, while the critical temperature related to the MIT without thermally induced hysteresis was achieved for $x = 0$ – 0.8 . The linearity in the temperature dependence of resistivity across MIT of $\text{Nd}_x\text{Sm}_{1-x}\text{NiO}_3$ was achieved by paralleling a constant resistor, while the magnitudes of such parallel resistors compared with $\text{Nd}_x\text{Sm}_{1-x}\text{NiO}_3$ were presented. The entire temperature range of 210–360 K can be covered by integrating the $\text{Nd}_x\text{Sm}_{1-x}\text{NiO}_3$ with different Nd/Sm atomic ratios from $x = 0.2$ to $x = 0.8$. Compared with conventional NTCR materials, such array-like $\text{Nd}_x\text{Sm}_{1-x}\text{NiO}_3$ achieves higher magnitudes of TCR (e.g., 7%–14%), and this is anticipated to be of utility in accurate temperature sensing at low-temperature ranges.

Acknowledgements

This work was financially supported by the National Key Research and Development Program of China (No. 2021YFA0718900) and the National Natural Science Foundation of China (No. 62074014). Jikun Chen also acknowledges the Xiaomi scholarship.

Conflict of Interest

We declare no competing financial interest.

Supplementary Information

The online version contains supplementary material available at <https://doi.org/10.1007/s12613-023-2816-1>.

References

- [1] J.K. Chen, H.Y. Hu, J.O. Wang, *et al.*, A d-band electron correlated thermoelectric thermistor established in metastable per-

- ovskite family of rare-earth nickelates, *ACS Appl. Mater. Interfaces*, 11(2019), No. 37, p. 34128.
- [2] S.D. Ha, J. Shi, Y. Meroz, L. Mahadevan, and S. Ramanathan, Neuromimetic circuits with synaptic devices based on strongly correlated electron systems, *Phys. Rev. Appl.*, 2(2014), No. 6, art. No. 064003.
- [3] H.T. Zhang, T.J. Park, I.A. Zaluzhnyy, *et al.*, Perovskite neural trees, *Nat. Commun.*, 11(2020), No. 1, art. No. 2245.
- [4] F. Zuo, P. Panda, M. Kotiuga, *et al.*, Habituation based synaptic plasticity and organismic learning in a quantum perovskite, *Nat. Commun.*, 8(2017), No. 1, art. No. 240.
- [5] F. Guo, S. Chen, Z. Chen, *et al.*, Printed smart photovoltaic window integrated with an energy-saving thermochromic layer, *Adv. Opt. Mater.*, 3(2015), No. 11, p. 1524.
- [6] X. Deng, S.Q. Wang, Y.X. Liu, *et al.*, A flexible Mott synaptic transistor for nociceptor simulation and neuromorphic computing, *Adv. Funct. Mater.*, 31(2021), No. 23, art. No. 2101099.
- [7] Z.A. Li, F.B. Yan, X.Y. Li, *et al.*, Molten-salt synthesis of rare-earth nickelate electronic transition semiconductors at medium high metastability, *Scripta Mater.*, 207(2022), art. No. 114271.
- [8] D. Li, K. Lee, B.Y. Wang, *et al.*, Superconductivity in an infinite-layer nickelate, *Nature*, 572(2019), No. 7771, p. 624.
- [9] S. Hyeon Lee, M. Kim, S.D. Ha, J.W. Lee, S. Ramanathan, and S. Tiwari, Space charge polarization induced memory in SmNiO₃/Si transistors, *Appl. Phys. Lett.*, 102(2013), No. 7, art. No. 072102.
- [10] S.H. Misha, N. Tamanna, A. Prakash, *et al.*, Comprehensive analysis of electro thermally driven nanoscale insulator-metal transition SmNiO₃-based selector for cross-point memory array, *Jpn. J. Appl. Phys.*, 54(2015), No. 4S, art. No. 04DD09.
- [11] K. Ramadoss, F. Zuo, Y.F. Sun, *et al.*, Proton-doped strongly correlated perovskite nickelate memory devices, *IEEE Electron Device Lett.*, 39(2018), No. 10, p. 1500.
- [12] J. Shi, S.D. Ha, Y. Zhou, F. Schoofs, and S. Ramanathan, A correlated nickelate synaptic transistor, *Nat. Commun.*, 4(2013), art. No. 2676.
- [13] C. Oh, M. Jo, and J. Son, All-solid-state synaptic transistors with high-temperature stability using proton pump gating of strongly correlated materials, *ACS Appl. Mater. Interfaces*, 11(2019), No. 17, p. 15733.
- [14] Y.Y. Tian, S.H. Wang, G. Li, *et al.*, Magnetization reorientation induced by spin-orbit torque in YIG/Pt bilayers, *Chin. Phys. B*, 29(2020), No. 11, art. No. 117504.
- [15] H.T. Zhang, T.J. Park, A.N.M.N. Islam, *et al.*, Reconfigurable perovskite nickelate electronics for artificial intelligence, *Science*, 375(2022), No. 6580, p. 533.
- [16] J.K. Chen, Z.A. Li, H.L. Dong, *et al.*, Pressure induced unstable electronic states upon correlated nickelates metastable perovskites as batch synthesized via heterogeneous nucleation, *Adv. Funct. Mater.*, 30(2020), No. 23, art. No. 2000987.
- [17] X.Y. Li, Z.A. Li, F.B. Yan, *et al.*, Batch synthesis of rare-earth nickelates electronic phase transition perovskites via rare-earth processing intermediates, *Rare Met.*, 41(2022), No. 10, p. 3495.
- [18] H.Y. Li, Y.Z. Wang, F.Q. Meng, *et al.*, Metal-organic decomposition growth of thin film metastable perovskite nickelates with kinetically improved quantum transitions, *Int. J. Miner. Metall. Mater.*, 30(2023), No. 12, p. 2441.
- [19] F.B. Yan, Z.S. Mi, J.H. Chen, *et al.*, Revealing the role of interfacial heterogeneous nucleation in the metastable thin film growth of rare-earth nickelate electronic transition materials, *Phys. Chem. Chem. Phys.*, 24(2022), No. 16, p. 9333.
- [20] Y.M. Klein, M. Kozłowski, A. Linden, P. Lacorre, M. Medarde, and D.J. Gawryluk, RENiO₃ single crystals (RE = Nd, Sm, Gd, Dy, Y, Ho, Er, Lu) grown from molten salts under 2000 bar of oxygen gas pressure, *Cryst. Growth Des.*, 21(2021), No. 7, p. 4230.
- [21] J.R. Li, R.J. Green, Z. Zhang, *et al.*, Sudden collapse of magnetic order in oxygen-deficient nickelate films, *Phys. Rev. Lett.*, 126(2021), No. 18, art. No. 187602.
- [22] J.K. Chen, H.Y. Hu, J.O. Wang, *et al.*, Overcoming synthetic metastabilities and revealing metal-to-insulator transition & thermistor bi-functionalities for d-band correlation perovskite nickelates, *Mater. Horiz.*, 6(2019), No. 4, p. 788.
- [23] H. Zhang, Z. Li, T. Zhang, *et al.*, Improvement of metal-insulator transition and mechanical strength of RENiO₃ by co-sintering, *J. Appl. Phys.*, 134(2023), No. 13, art. No. 135104.
- [24] W.J. Mao, Y.M. Jia, J. Wu, *et al.*, Optical temperature sensing of piezoelectric Er³⁺-doped (Ba_{0.97}Ca_{0.03})(Sn_{0.06}Ti_{0.94})O₃ ceramic, *Funct. Mater. Lett.*, 9(2016), No. 5, art. No. 1650060.